Appl Phys A (2011) 104:781–792
DOI 10.1007/s00339-011-6436-7

Applied Physics A
Materials Science & Processing

Runaway lattice-mismatched interface in an atomistic simulation of femtosecond laser irradiation of Ag film–Cu substrate system

Chengping Wu · Derek A. Thomas · Zhibin Lin · Leonid V. Zhigilei

Received: 22 September 2010 / Accepted: 8 April 2011 / Published online: 15 May 2011

Abstract The atomic mixing and structural transformations in a Ag film–Cu substrate system irradiated by a femtosecond laser pulse are investigated in a simulation performed with a model that couples the classical molecular dynamics method with a continuum-level description of the laser excitation and subsequent relaxation of the conduction-band electrons. The higher strength of the electron–phonon coupling in Cu compared to Ag results in preferential subsurface heating and melting of the Cu substrate. The melting is followed by fast cooling and rapid resolidification occurring under conditions of strong undercooling below the equilibrium melting temperatures of Cu and Ag. The rapid resolidification results in a complex structure of the interfacial region, where the lattice-mismatched interface is separated from the Ag–Cu mixing region by an intermediate pseudomorphic bcc Cu layer that grows epitaxially on the (001) face of the fcc Ag film during the final stage of the resolidification process. The new lattice-mismatched interface has a three-dimensional structure consisting of a periodic array of stacking fault pyramids outlined by stair-rod partial dislocations. The intermediate bcc layer and the stacking fault pyramid structure of the mismatched interface are likely to present a strong barrier for dislocation propagation, resulting in the effective hardening of the layered structure treated by the laser irradiation. The concentration profiles in the atomic mixing region are substantially wider compared to the width of the equilibrium Cu–Ag interface and have a pronounced asymmetric shape that reflects the preferential melting of the Cu substrate.

C. Wu · D.A. Thomas · Z. Lin · L.V. Zhigilei (✉)
Department of Materials Science and Engineering, University of Virginia, 395 McCormick Road, Charlottesville, VA 22904-4745, USA
e-mail: lz2n@virginia.edu
Fax: +1-434-9825660

Present address:
D.A. Thomas
Faculty of Engineering, University of Tokyo, Tokyo, Japan

Present address:
Z. Lin
Department of Physics, Renewable Energy Materials Research Science and Engineering Center (REMRSEC), Colorado School of Mines, Golden, CO, USA

1 Introduction

Rapid progress in the development of accessible sources of short (pico- and femtosecond) laser pulses opens up new opportunities for surface modification with high accuracy and spatial resolution. In particular, the shallow depth of the heat-affected zone in short-pulse laser processing of strongly absorbing materials can result in the confinement of the laser-induced structural modifications within a surface layer as small as tens of nanometers, e.g. [1–5]. The small size of the laser-modified region makes experimental characterization of laser-induced structural changes challenging and, at the same time, increases the importance of understanding the generation, mobility, interactions, and stability of individual crystal defects.

The fast and highly localized energy deposition in short-pulse laser processing unavoidably creates the conditions of strong thermodynamic, electronic, and mechanical non-equilibrium, making the theoretical description of the structural transformations difficult. For multi-component and composite targets, an additional challenge is to provide an adequate description of the mass transfer and compositional changes in the transiently heated and melted surface region. The conventional analysis of the atomic diffusion and thermodynamic driving forces [6, 7] is hardly applicable to systems experiencing a very fast melting–resolidification cycle.

Atomic-level computer modeling has the ability to provide detailed information on the complex structural and phase transformations induced by short-pulse laser irradiation [8–19] and can assist in the advancement of laser-driven applications. In particular, recent atomistic simulations of laser interactions with metal targets provided insights into the mechanisms and driving forces responsible for the generation of point defects (vacancies and interstitials) in Cr targets [14], revealed the processes responsible for the formation of a nanocrystalline structure in regions of localized photoexcitation of metal films [16], clarified the effect of the grain boundaries on the kinetics of laser melting of nanocrystalline Au films [17], and helped to establish the connections between the maximum melting depth, photomechanical spallation, and phase explosion in short-pulse laser interactions with metal targets [18]. First simulations of laser interactions with layered metal targets have also been reported for Au films deposited on a bulk Cu substrate [19]. The initial energy redistribution and the depth of the region undergoing melting and resolidification are found to be strongly affected by the difference in the strength of electron–phonon coupling of the film and substrate materials and by the transient variations of the electron–phonon coupling related to the thermal excitation of lower band electrons [20].

In this paper, we report the results of an atomic-level simulation of a femtosecond laser interaction with a layered Ag film–Cu substrate target. Thermodynamically, the Ag–Cu binary system is characterized by a positive heat of mixing and an eutectic phase diagram, with virtually no mutual solubility at room temperature. In rapid quenching experiments, however, the metastable fcc solid solutions are commonly produced in the whole range of the alloy compositions, e.g. [21, 22]. The formation of the amorphous phase is not observed in liquid quenching experiments, but has been reported for vapor quenching (co-deposition of the two components to an amorphous substrate held at liquid nitrogen temperature) [23, 24], cold rolling of Ag and Cu multi-layers [25], and picosecond laser quenching [26]. The extreme heating and cooling conditions realized in short-pulse laser processing experiments suggest feasibility of generation of non-equilibrium compositional profiles and metastable phases in the interfacial region of the layered Ag–Cu target. While a detailed analysis of the atomic mixing and structural transformations occurring in the layered targets under different irradiation conditions will be presented elsewhere, a particular focus of this paper is on an unusual effect of a 'runaway' lattice-mismatched interface, when the misfit dislocations associated with the lattice-mismatched interface separate from the Ag–Cu mixing region and shift into the Cu substrate as a result of the resolidification process occurring under conditions of strong undercooling. A brief description of the computational model used in the simulations is given in Sect. 2. The results of the simulation and a detailed structural analysis of the laser-treated target are presented and discussed in Sect. 3 and are summarized in Sect. 4.

2 Computational model

The atomic mixing and structural changes generated by short-pulse laser irradiation are simulated for a system consisting of a 30-nm Ag film deposited on a bulk Cu substrate. The simulation is performed with a combined atomistic–continuum model [9, 18] that couples the classical molecular dynamics (MD) method with a continuum-level description of the laser excitation and subsequent relaxation of the conduction-band electrons. The model accounts for the fast electron heat conduction in the metal target and provides an adequate representation of the fast heating and cooling of the surface region of the target. A complete description of the combined atomistic–continuum model is given in [9, 18], whereas the computational setup used in the simulation is similar to the one used for the Cu–Au system in [19]. Briefly, the atomic-level MD representation is used only for the top 230-nm part of the target (30-nm Ag film and a top 200-nm part of the Cu substrate), whereas the heat transfer in the deeper part of the target is described by coupled electron and lattice heat conduction equations (two-temperature model (TTM) [27]) solved down to the depth of 2.4 μm. This depth is chosen so that no significant increase in the electron or lattice temperatures is observed at the bottom of the computational domain during the time of the simulation.

The interatomic interactions in the MD part of the system are described by the embedded atom method (EAM) potential in the form suggested by Foiles, Baskes, and Daw (FBD) [28]. The potential functions for pure elements are fitted to the equilibrium lattice constants, sublimation energies, bulk moduli, elastic constants, and vacancy formation energies, whereas the parameters of functions describing the Ag–Cu cross-interaction are fitted to the heat of mixing of dilute solid solutions. Our implementation of the FBD EAM potential includes a cutoff function [29] that smoothly brings the interaction energies and forces to zero at a cutoff distance of 5.5 Å.

The equilibrium melting temperatures of pure Ag (1,139 ± 2 K) and Cu (1288 ± 2 K) are calculated in liquid-crystal coexistence simulations performed at zero pressure for a system consisting of 5760 atoms ($6 \times 6 \times 40$ unit cells), with liquid-crystal interface oriented along the (001) plane of the fcc crystal. The hydrostatic zero pressure conditions are ensured by independent control over the three diagonal components of the stress tensor. The error of ±2 K is obtained by running series of simulations at different temperatures and monitoring the evolution of the liquid-crystal

interface for 2 ns. The temperatures in the simulations were varied around the melting temperatures listed above with a step of 1 K. The growth or disappearance of the liquid phase is reproducible outside the ±2 K intervals around the melting temperatures, whereas within these intervals the dominance of melting or solidification is not apparent. The values of the melting temperatures are in a reasonable agreement with the results of earlier coexistence calculations performed with the same potential [30, 31], where the values of 1144 K for Ag and 1279 K for Cu are obtained. The melting temperatures predicted by the FBD EAM are within 7% of the experimental values of 1235 K for Ag and 1356 K for Cu [32] and have a similar relation, the melting temperature of Cu being slightly higher than the one of Ag. Moreover, the high-temperature [30] and low-temperature [33–35] parts of the Ag–Cu phase diagram calculated with the FBD EAM potential are in a good semi-quantitative agreement with the experimental eutectic phase diagram of this system. The small positive deviation of the lattice parameter of the Ag–Cu solid solution from Vegard's law, predicted with the FBD EAM potential, is also consistent with experimental data obtained for the metastable fcc phase formed by rapid quenching [33]. We conclude, therefore, that the FBD EAM potential is appropriate for the investigation of short-pulse laser processing of the Ag–Cu layered system.

The top 200-nm part of the Cu substrate and the 30-nm Ag film in the initial system are represented by fcc crystallites with lateral dimensions of 3.27 nm × 3.27 nm at 300 K and periodic boundary conditions imposed in the directions parallel to the surface of the target. At the bottom of the MD part of the model, a special pressure-transmitting boundary condition [36, 37] is applied in order to avoid an artificial reflection of the laser-induced pressure wave generated in the surface region by the fast laser energy deposition. The film and the target have the same crystallographic orientation, with (001) planes oriented parallel to the surface of the target. Although the FBD EAM potential is fitted to the room-temperature values of lattice constants and other parameters [28], the fitting is done using static calculations that do not account for the thermal expansion from zero to room temperature. As a result, the potential overpredicts the finite-temperature values of the lattice parameters, e.g. $a_{\mathrm{Cu}} = 3.63$ Å and $a_{\mathrm{Ag}} = 4.11$ Å are determined in constant zero pressure MD simulations performed at 300 K (compared to the experimental values $a_{\mathrm{Cu}} = 3.61$ Å and $a_{\mathrm{Ag}} = 4.09$ Å [38]). Nevertheless, the relative values of the lattice parameters and the corresponding misfit are similar for both experimental values and the MD results at 300 K, $9a_{\mathrm{Cu}} = 7.95a_{\mathrm{Ag}}$ and $(a_{\mathrm{Ag}} - a_{\mathrm{Cu}})/a_{\mathrm{Cu}} = 0.13$, suggesting that the discrepancy between the calculated and experimental lattice parameters does not affect the properties of the Cu–Ag interface.

The lateral size of the computational system corresponds to nine fcc unit cells in each direction for the Cu substrate and eight slightly compressed fcc unit cells for the Ag film at 300 K. Before applying laser irradiation, the initial system is equilibrated in a MD simulation performed at 300 K for 100 ps. The equilibration results in the formation of a semicoherent interface with an array of misfit dislocations parallel to ⟨110⟩ directions in the plane of the interface. The atomic structure of the interface is shown in Fig. 1, where the atoms are colored by their type in Fig. 1a and based on the output of the modified version[1] of the structural analysis suggested in [39] in Fig. 1b. The latter representation allows for an easy identification of the network of misfit dislocations, with atoms that belong to the dislocation cores colored yellow and green.

The electron temperature dependences of the thermophysical material properties included in the TTM equation for the electron temperature (electron–phonon coupling factor and electron heat capacity) are taken in the form that accounts for the thermal excitation from the electron states below the Fermi level [20, 40]. The electron thermal conductivity is described by the Drude model relationship, $K_{\mathrm{e}}(T_{\mathrm{e}}, T_{\mathrm{l}}) = v^2 C_{\mathrm{e}}(T_{\mathrm{e}})\tau_{\mathrm{e}}(T_{\mathrm{e}}, T_{\mathrm{l}})/3$, where $C_{\mathrm{e}}(T_{\mathrm{e}})$ is the electron heat capacity, v^2 is the mean square velocity of the electrons contributing to the electron heat conductivity, approximated in this work as the Fermi velocity squared, ${v_{\mathrm{F}}}^2$, and $\tau_{\mathrm{e}}(T_{\mathrm{e}}, T_{\mathrm{l}})$ is the total electron scattering time defined by the electron–electron and electron–phonon scattering rates, $1/\tau_{\mathrm{e}} = 1/\tau_{\mathrm{e-e}} + 1/\tau_{\mathrm{e-ph}} = AT_{\mathrm{e}}^2 + BT_{\mathrm{l}}$. The values of the coefficient A (2.66×10^6 s^{-1} K^{-2} for Cu and 3.57×10^6 s^{-1} K^{-2} for Ag) are estimated within the free electron model, following the approach suggested in [41]. The values of the coefficient B (2.41×10^{11} s^{-1} K^{-1} for Cu and 1.12×10^{11} s^{-1} K^{-1} for Ag) are obtained from the experimental values of the thermal conductivity of solid Cu and Ag at the melting temperature, 330 W m^{-1} K^{-1} for Cu and 363 W m^{-1} K^{-1} for Ag [42]. In the region adjacent to the Cu–Ag interface, the material properties included in the TTM equation for the electron temperature are calculated as linear combinations of the properties of individual components taken with weights equal to the local atomic concentrations.

[1] To avoid misidentification of crystalline structures due to small lattice distortions, the following changes have been made to the method suggested in [39]: the neighbor radii used for finding neighboring atoms are extended from $r_{ij}^2 < 1.45r_0^2$ to $r_{ij}^2 < 1.69r_0^2$ for N_0 neighbors, and from $r_{ij}^2 < 1.55r_0^2$ to $r_{ij}^2 < 1.76r_0^2$ for N_1 neighbors; the maximum $\cos\theta_{jik}$ for χ_3 in Table I is changed from −0.705 to −0.195; in step (v) of Table II, $\chi_0 > 0$ is changed to $\chi_7 > 0$; in step (vi) of Table II, the condition for fcc atoms $\chi_0 = 6$ is made stronger by adding an additional condition $\chi_0 + \chi_1 + \chi_2 + \chi_3 = 30$, and the condition for bcc atoms $\chi_0 = 7$ is made stronger by adding an additional condition $\chi_0 + \chi_1 + \chi_2 + \chi_3 > 30$; the expression $\delta_{\mathrm{hcp}} = (|\chi_0 - 3| + |\chi_0 + \chi_1 + \chi_2 + \chi_3 - 9|)/12$ is changed to $\delta_{\mathrm{hcp}} = (|\chi_0 - 3| + |\chi_0 + \chi_1 + \chi_2 - 9|)/12$.

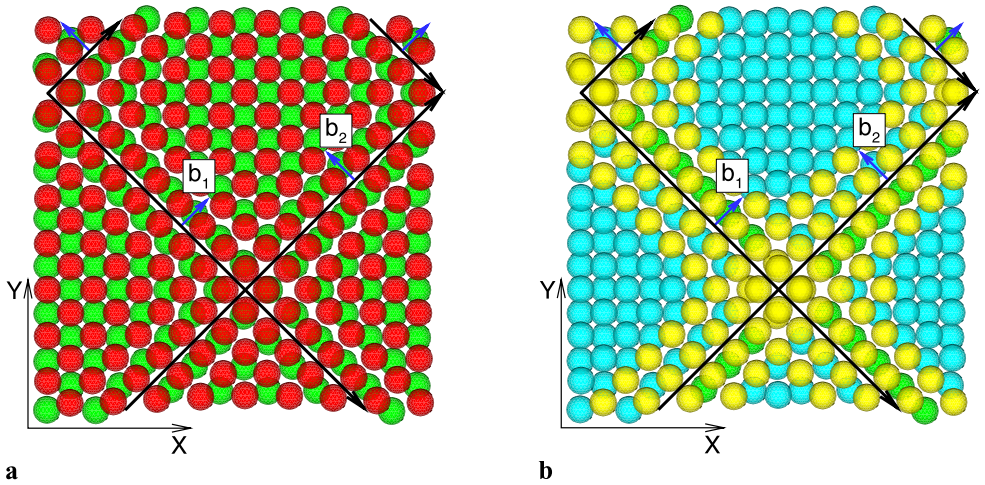

Fig. 1 Initial configuration of the Cu–Ag interface equilibrated at 300 K. Two atomic layers adjacent to the interface are shown, with atoms *colored* by their type (*red* for Cu and *green* for Ag) in (**a**) and based on the output of the structural analysis suggested in [39] (see footnote 1) (*light blue* and *green* atoms belong to atomic configurations that correspond to fcc and hcp structures, respectively; the structure around the *yellow* atoms cannot be assigned to any crystal structure) in (**b**). The *lines* of misfit dislocations are shown by *black arrows* with small *blue arrows* indicating the corresponding Burgers vectors, $\vec{b}_1 = \frac{1}{2}[110]$ and $\vec{b}_2 = \frac{1}{2}[\bar{1}10]$

The irradiation of the layered target with a 200-fs laser pulse is represented through a source term added to the equation for the electron temperature. The source term simulates excitation of the conduction-band electrons by a laser pulse with a Gaussian temporal profile and reproduces the exponential attenuation of laser intensity with depth under the surface (Beer–Lambert law). In order to account for the ballistic energy transport occurring before the thermalization of the excited electrons [19, 43, 44], the optical absorption depth, λ_{opt}, is substituted in the source term by an effective range of the laser energy deposition, $\lambda_{opt} + \lambda_{ball}$ [9, 19, 43]. The strong dependence of the electron–electron scattering on the excitation energy [44] and modification of the scattering rates in the Ag–Cu interfacial region introduce uncertainty to the estimation of the effective depth of the ballistic energy transport [19]. In the simulation reported in this paper, we assume the effective range of the laser energy deposition to be $\lambda_{opt} + \lambda_{ball} = 100$ nm. As shown in [19] for the Au–Cu system, the variation of $\lambda_{opt} + \lambda_{ball}$ affects the values of laser fluence required for the onset of the interfacial melting or complete melting of the film, but does not change the qualitative picture of the laser-induced processes.

3 Results and discussion

3.1 Laser heating and sub-surface melting

The simulation discussed in this paper is performed for the layered Cu–Ag system irradiated by a 200-fs laser pulse at an absorbed fluence of 130 mJ/cm^2. This fluence is ∼1.3 times higher than the fluence required for the onset of sub-surface melting of the interfacial region (∼100 mJ/cm^2) and ∼1.2 times lower than the threshold fluence for photomechanical spallation [45] of the Ag film from the Cu substrate (∼160 mJ/cm^2). The contour plots in Fig. 2 show the evolution of the lattice temperature, pressure, and density in the irradiated target. Although immediately after the laser pulse the electron temperature in the Ag film is substantially higher than the one in the underlying Cu substrate, the lattice temperature increases faster at the Cu side of the Cu–Ag interface, Fig. 2a. This preferential sub-surface heating can be explained by substantially stronger electron–phonon coupling in Cu compared to Ag (room-temperature values of the electron–phonon coupling factor are $\sim 5.5 \times 10^{16}$ W m^{-3} K^{-1} for Cu and $\sim 2.5 \times 10^{16}$ W m^{-3} K^{-1} for Ag and the difference becomes larger with increasing electron temperature due to the stronger contribution of thermally excited d-band electrons in the case of Cu [20]). A similar effect of sub-surface heating in femtosecond laser interactions with layered targets has been predicted in TTM calculations performed for Cr–Au targets [46] and in TTM-MD simulations of Cu–Au targets [19]. In both cases, the faster increase of the lattice temperature in the Cr or Cu layers was attributed to the stronger electron–phonon coupling in Cr and Cu compared to Au.

The rapid heating of the upper part of the Cu substrate leads to the build up of high compressive stresses that drive compressive pressure waves deeper into the bulk of the target and in the direction of the free surface, Fig. 2b. The reflection of the wave from the free surface of the Ag film transforms it to an unloading tensile wave that follows the compressive wave propagating into the bulk of the Cu

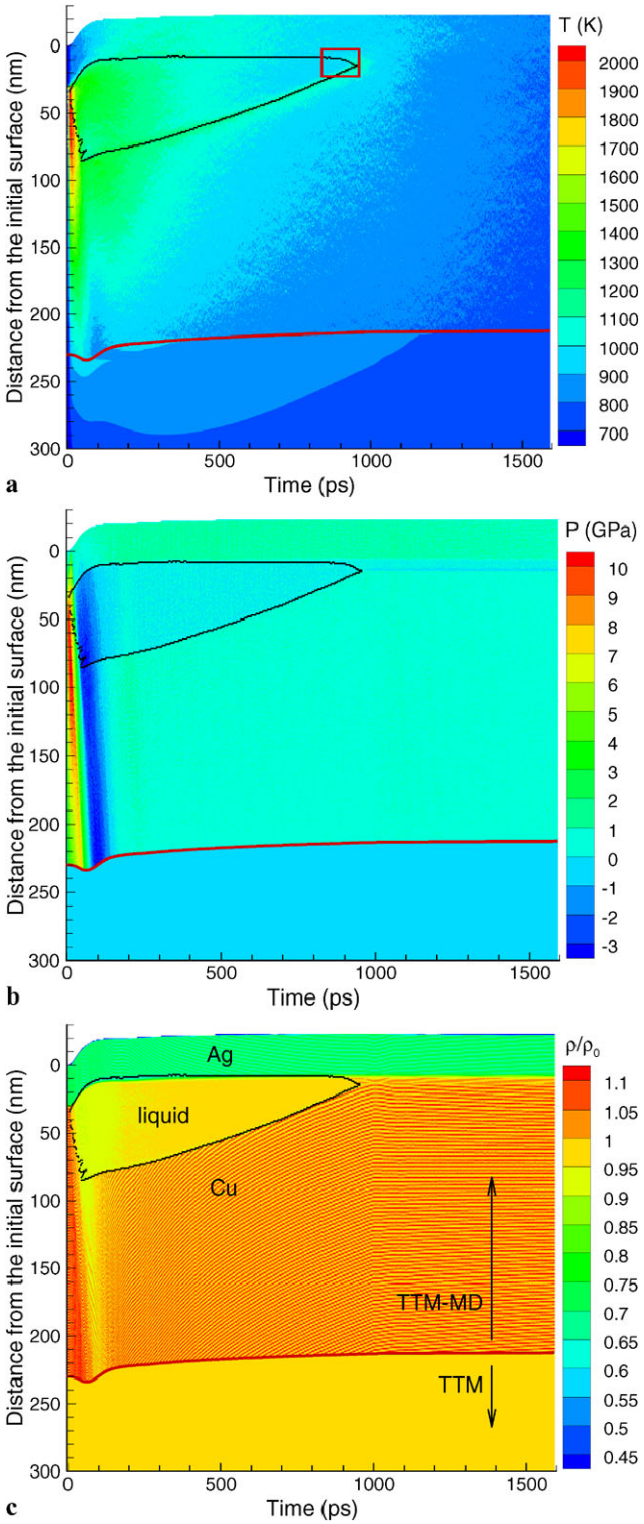

◀ **Fig. 2** Contour plots of the lattice temperature (**a**), pressure (**b**), and density (**c**) for a simulation of a Cu–Ag target irradiated with a 200-fs laser pulse at an absorbed fluence of 130 mJ/cm^2. The laser pulse is directed along the *Y*-axis, from the *top* of the contour plots. The *black lines* separate the melted regions from the crystalline parts of the target. The *red lines* separate the atomistic (TTM-MD) and continuum (TTM) parts of the computational domain. The *red rectangle* in (**a**) shows the region and time interval for which snapshots are shown in Fig. 4. The density scale in (**c**) is normalized to the density of Cu before the irradiation (at 300 K), ρ_0. The fine 'fingerprint'-type pattern observed in the crystalline parts of the target in the density plot is an artifact of the data analysis method—the physical properties are averaged over 1-nm-thick slices and the stepwise variation of the number of atoms (and density) in each slice corresponds to an atomic layer entering/leaving the slice due to the material displacement in response to the pressure waves and thermal expansion

substrate. Both compressive and tensile components of the laser-generated pressure wave are transmitted through the pressure-transmitting boundary at the bottom of the atomistic part of the computational model without any noticeable reflection.

The rising lattice temperature in the top part of the substrate quickly exceeds the melting temperature of Cu and leads to the fast homogeneous melting of a ∼55-nm region of the substrate. The melted part of the target is outlined by the black lines in Fig. 2 and is particularly apparent in the density plot (Fig. 2c), where the difference in densities of liquid Cu, solid Cu, and solid Ag makes it easy to distinguish the melted region from the rest of the substrate. Similarly, the boundary of the melted region can be identified by a jump in the level of pressure in Fig. 2b. The hydrostatic pressure conditions and complete relaxation of stresses are quickly achieved in the melted part of the substrate, whereas the laser-induced compressive stresses in the crystalline part of the target cannot completely relax by the uniaxial expansion in the direction normal to the surface. The uniaxial expansion of the crystalline part of the target results in anisotropic lattice deformations and corresponding quasi-static anisotropic stresses that slowly decrease with cooling of the surface region by heat conduction to the bulk of the target.

The melting starts just below the Cu–Ag interface at ∼10 ps and continues during the following 40 ps, reaching the maximum depth of ∼85 nm below the initial position of the surface of the target. The nucleation of the liquid regions at the end of the melting process is assisted by the tensile stresses associated with the unloading wave propagating through the melting region. A relatively small (∼3-nm deep) part of the Ag film adjacent to the Cu–Ag interface also undergoes melting.

3.2 Cooling and resolidification

The strong temperature gradient and the fast electronic heat conduction in Cu lead to the rapid cooling of the surface region of the irradiated target and, by the time of 100 ps, the temperature in the whole melted region drops below the equilibrium melting temperature of Cu. The velocity of the resolidification front increases with increasing undercooling of the melted Cu and reaches the maximum velocity of ∼100 m/s by the time of ∼700 ps, Fig. 2.

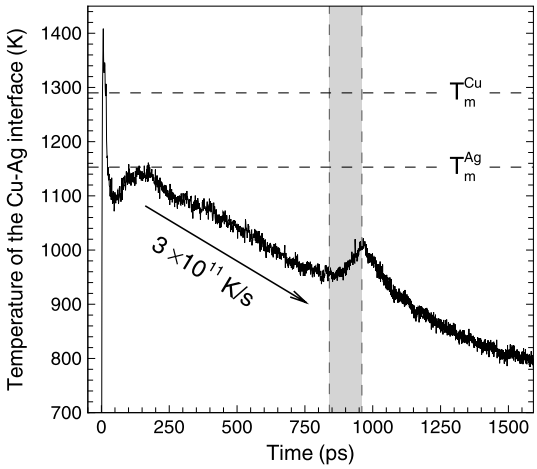

Fig. 3 Time dependence of the lattice temperature of the interfacial region of a Cu–Ag target irradiated with a 200-fs laser pulse at an absorbed fluence of 130 mJ/cm^2. The horizontal *dashed lines* show the equilibrium melting temperatures of the FBD EAM Cu and Ag materials. The lattice temperature is calculated from the average kinetic energy of atoms in a 5-nm layer adjacent to the interface. The *gray area* marks the time interval from 840 to 960 ps, during which a resolidification front propagates through the region of atomic mixing from the side of the Ag film and meets another resolidification front that propagates from the side of the Cu substrate (see Fig. 4). The release of the latent heat of melting upon solidification of the interfacial region is responsible for the transient temperature increase during the time of the solidification

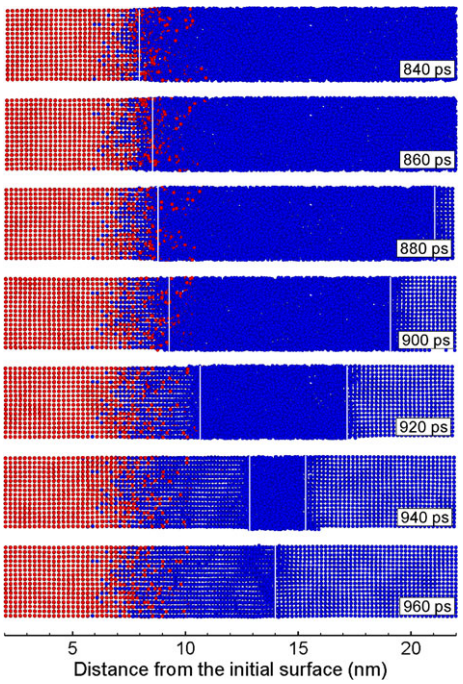

Fig. 4 Snapshots of the evolution of the atomic structure in the region of the Cu–Ag interface in the simulation illustrated by the contour plots in Fig. 2. The snapshots are taken for the region and the time interval marked in Fig. 2a by the *red rectangle*. Atoms are *colored* according to their type—Ag atoms are colored *red* and Cu atoms are colored *blue*. To reduce the thermal noise in atomic positions, the configurations are quenched for 0.2 ps using a velocity dampening technique (see text). The fast quenching does not introduce any structural changes to the atomic configurations but makes the visual analysis more straightforward. The *vertical white lines* in each snapshot show the approximate locations of resolidification fronts propagating from the Ag (*left*) and Cu (*right*) sides of the system and meeting each other at ∼955 ps

From the Ag side of the melted region, a noticeable advancement of the resolidification front is observed only starting from ∼400 ps, when the temperature of the Cu–Ag interface drops down to ∼1,080 K, Fig. 3. This second resolidification front propagates with a relatively low average velocity of ∼8 m/s for ∼275 ps (until the time of ∼675 ps) and then slows down and remains almost immobile for the following ∼165 ps. The low velocity of the second resolidification front can be explained by slower solidification kinetics in binary systems and, more importantly, by the depression of the melting temperature (liquidus line) with respect to the pure Ag and Cu. The range of diffusional mixing of Cu and Ag atoms quickly extends up to the solid part of the Ag film and the resolidification front propagates through the melt with increasing concentration of Cu atoms. The propagation of the resolidification comes to a temporal halt at ∼675 ps, when the composition of the melt becomes close to the eutectic composition of ∼36 at.% Cu estimated for the FBD EAM Cu–Ag system [30].

While the resolidification front from the Ag side remains stuck in the mixing region and the resolidification front from the Cu side propagates at its maximum velocity, the temperature of the Cu–Ag interface continues to decrease with the cooling rate of $\sim 3 \times 10^{11}$ K/s, Fig. 3. Finally, when at ∼840 ps the temperature of the interface drops down to ∼950 K (close to the estimated eutectic temperature of 904 K [30]), the resolidification front on the Ag side starts to move again and slowly, with an average velocity of ∼25 m/s, passes through the remaining part of the mixing region within the following 60 ps. After crossing the mixing region, the resolidification front sharply accelerates and propagates through the undercooled Cu with a velocity similar to the one of the resolidification front propagating from the Cu substrate, ∼100 m/s. The atomic-level view of the resolidification process in the vicinity of the mixing region is provided by snapshots of atomic configurations shown in Fig. 4, where the positions of the two resolidification fronts are marked by white vertical lines. The two resolidification fronts meet each other at ∼955 ps and form a new lattice-mismatched interface at a distance of ∼6.5 nm from the center of the mixing region. This new mismatched interface is remarkable, since it is located inside the Cu substrate and is separating the bulk of the fcc Cu substrate from an intermediate Cu layer with a structure that forms as a result of the pseudomorphic epitaxial growth on (001) Ag. The structure of the new mismatched interface, the intermediate Cu layer, and the factors that facilitate the epitaxial growth of Cu on the Ag lattice are discussed below.

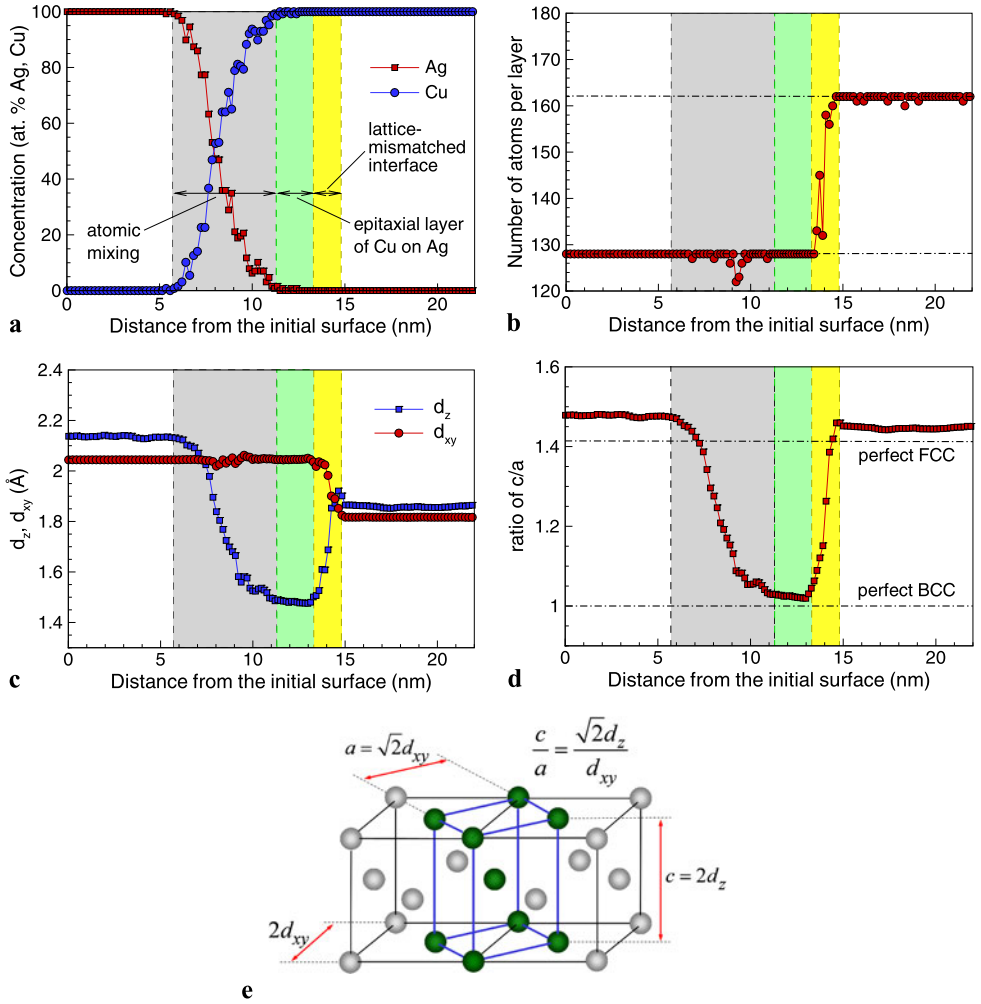

Fig. 5 Concentration profiles (**a**), number of atoms in atomic planes (**b**), spacing between {200} planes of the original fcc structure (**c**), and ratio c/a of the bct lattice constants (**d**) shown for a region adjacent to the Ag–Cu interface. The analysis is performed for an atomic configuration obtained by the end of the simulation (1.59 ns after the laser pulse) and quenched by applying the velocity dampening technique for 0.2 ps (the snapshots of the corresponding atomic configurations are shown in Fig. 6a–c). The definitions of the structural parameters shown in the plots are illustrated in (**e**). Each point in (**a**) and (**b**) is calculated for an individual atomic plane parallel to the surface of the layered system. The atomic planes correspond to (002) planes in the original fcc structures of the Cu substrate and the Ag film. In (**c**), d_{xy} corresponds to the average spacing between the neighboring atomic planes that correspond to (200) and (020) planes in the fcc structure, d_z corresponds to the average spacing between the neighboring (002) planes of the fcc structure, and atoms that do not belong to fcc or bcc/bct atomic configurations are excluded from the averaging. In (**d**), the ratio c/a is defined as shown in (**e**), so that the perfect fcc and bcc structures are treated as general bct structures with ideal ratios of $c/a = \sqrt{2}$ and 1, respectively. The *gray*, *green*, and *yellow areas* in the plots mark the regions of atomic mixing, pseudomorphic epitaxial layer of Cu on Ag, and corrugated lattice-mismatched interface consisting of stacking fault pyramids illustrated in Fig. 7, respectively

3.3 Structure of the resolidified region

To better understand the unusual phenomenon of the 'runaway' lattice-mismatched interface, when the lattice-mismatched interface separates from the Ag–Cu mixing region and shifts into the Cu substrate, we consider the composition profiles and distributions of structural characteristics in a part of the target that includes both the atomic mixing region and the new lattice-mismatched interface, Fig. 5. The analysis is performed for an atomic configuration obtained by the end of the simulation, 1.59 ns after the laser pulse. The average composition and structural characteristics are calculated for individual atomic planes parallel to the surface of the layered system. These atomic planes correspond to (002) planes in the original fcc structures of the Cu substrate and Ag film. To reduce the thermal noise in atomic positions, the analysis is preceded by quenching of the atomic configuration for 0.2 ps using a velocity dampening technique, where the velocity of each individual atom is set to zero at the time when the kinetic energy of the atom maxi-

mizes. The fast quenching does not introduce any structural changes to the atomic configuration but makes the visualization and structural analysis more straightforward.

The concentration profiles produced by the laser processing of the layered target are shown in Fig. 5a. The width of the region of atomic mixing, shown as a gray area in Fig. 5, is ∼5.6 nm. This width is substantially wider compared to the width of the composition profiles predicted in Monte Carlo simulations for equilibrium interfaces, ∼1 nm [35]. The difference can be explained by the high rates of the cooling and resolidification processes realized in short-pulse laser processing. The high atomic mobility and unlimited solubility in the liquid state result in a rapid mixing in the transiently melted interfacial region. The subsequent fast resolidification happens within hundreds of picoseconds and does not allow for any significant compositional changes in the mixing region, thus resulting in the formation of non-equilibrium concentration profiles. The concentration profiles in Fig. 5a exhibit a noticeable asymmetry with respect to the location of the equal concentrations of Cu and Ag. The location where the concentration of the components is 50 at.% is shifted by ∼0.6 nm with respect to the center of the mixing region. The asymmetry in the concentration profiles can be attributed to the asymmetry in the interfacial melting that takes place mainly in the Cu substrate and only affects a shallow (up to 3 nm) part of the Ag film. The liquid-crystal interface provides a natural limit for the diffusion of Cu atoms into the Ag film and the advancement of the resolidification front from the Ag side confines the atomic mixing to an increasingly smaller part of the film. For example, one can see from the top snapshot in Fig. 4 that the Ag side of the interface has resolidified by the time of 840 ps, whereas the Cu side is still melted and is a subject of continued diffusion of Ag atoms into the Cu substrate.

The shift of the lattice-mismatched interface from the region of atomic mixing to the Cu substrate is apparent by comparing the concentration profiles in Fig. 5a with the distribution of the number of atoms per atomic monolayer shown in Fig. 5b. Even though there are almost no Ag atoms below the depth of ∼11 nm, the region where each layer consists of ∼128 atoms, as in the Ag crystal, extends down to ∼13.4 nm. The number of atoms per atomic layer jumps from 128 to 162, the value characteristic of the Cu fcc crystal, within a narrow region from 13.4 to 14.7 nm (marked by yellow color in Fig. 5), signifying the new location of the lattice-mismatched interface. A detailed discussion of the atomic structure of the mismatched interface is provided in Sect. 3.4.

Now we consider the structure of the intermediate 2-nm-wide region that separates the regions of Ag–Cu mixing and the new lattice-mismatched interface. As discussed in Sect. 3.2, the structure of this region, marked by green color in Fig. 5, is formed as a result of coherent epitaxial growth of Cu on Ag, with Cu atoms adopting the packing density of (002) planes of the Ag fcc lattice. Similarly to the number of atoms per atomic plane (Fig. 5b), the average spacing d_{xy} between the neighboring (200) or (020) planes, defined as shown in Fig. 5e, does not experience any noticeable change upon the transition from the Ag to the Cu part of the system and drops to the value characteristic of the Cu crystal only at the lattice-mismatched interface, Fig. 5c. On the contrary, the spacing d_z between the (002) atomic planes gradually decreases with decreasing concentration of Ag, saturates at an almost constant value of ∼1.48 Å in the region of the epitaxial layer of Cu on Ag, and increases to the value of the Cu substrate upon crossing the mismatched interface. The large disparity between the values of d_z and d_{xy} in the epitaxial layer suggests that the structure changes upon the transition through the mixing region.

In the regions away from the Ag–Cu intermixing and epitaxial layers, the difference in the levels of d_z and d_{xy} reflects the lateral confinement of the fcc lattice in the directions parallel to the surface of the irradiated target. The surface region of the target heated by the laser pulse can only expand in the direction normal to the surface, leading to the split between d_z that increases due to the relaxation of the z-component of thermoelastic stresses and d_{xy} that is fixed at its room-temperature value. The levels of the compressive stresses at a time of 1.59 ns after the laser pulse are $\sigma_{xx} = \sigma_{yy} = -0.6$ GPa on the Cu side of the lattice-mismatched interface and $\sigma_{xx} = \sigma_{yy} = -1.3$ GPa on the Ag side, above the atomic mixing region. The difference in the levels of the compressive stresses can be explained by the larger thermal expansion coefficient of Ag compared to Cu and the slightly compressed initial state of the Ag film at 300 K (see Sect. 2). The compressive stresses are also reflected in the pressure contour plot shown in Fig. 2b. The positive values of pressure, defined as a negative 1/3 of the first invariant of the stress tensor, $P = -(\sigma_{xx} + \sigma_{yy} + \sigma_{zz})/3$, contain contributions mainly from the first two diagonal components of the stress tensor, σ_{xx} and σ_{yy}.

The distinct decrease in the value of d_z upon the transition through the mixing region signifies the compression of the fcc lattice in the z direction and can be interpreted as a transformation from fcc to bcc structure along the so-called Bain path [47]. Both crystal structures can be represented by a body centered tetragonal (bct) structure with the ratio of bct lattice constants $c/a = \sqrt{2}$ for a perfect fcc structure and $c/a = 1$ for a perfect bcc structure, Fig. 5e. The change in the value of d_z (and the corresponding bct lattice parameter c) and the substitution of Ag atoms by 'smaller' Cu atoms upon crossing the mixing region result in a gradual transformation of the structure from laterally compressed fcc structure of Ag to a bcc lattice composed of Cu atoms. The bcc structure is slightly compressed in x and y directions since the lattice parameter of the bcc structure is fixed at a value of

$d_{xy}^{Ag}\sqrt{2} = 2.89$ Å and the lattice parameter of the metastable bcc Cu predicted for a temperature of 800 K by the FBD EAM potential is 2.91 Å (see below). The transition from the fcc Ag to the bcc Cu structure is apparent from the spatial variation of the c/a ratio shown in Fig. 5d, where the values of the c/a ratio that correspond to the perfect fcc and bcc lattices are marked by horizontal lines. The analysis of the local atomic structure also supports the conclusion on the bcc structure of the epitaxial layer located between the atomic mixing region and the displaced misfit interface. In the snapshots of the atomic configuration shown in Fig. 6b and c, the atoms are colored according to the local atomic structure and most of the atoms in the epitaxial layer are identified as bcc atoms.

The observation of the bcc structure of the epitaxial layer can be related to the results of experimental [48, 49] and computational [50] investigations of thin Cu films deposited on a Ag (001) substrate, where a pseudomorphic growth of bcc Cu is observed for film thicknesses of up to 10 monolayers. A good match between the lattice parameter of the bcc Cu structure and the first-neighbor distance in the fcc Ag structure, combined with a relatively small energy difference between the fcc and bcc Cu structures (the difference in the cohesive energies of the two structures predicted with the FBD EAM potential is 22 meV/atom, which is comparable to 20–40 meV/atom predicted in *ab initio* calculations [51, 52]) are the factors that facilitate the pseudomorphic epitaxial growth of the bcc Cu layer on the (001) face of the Ag crystal.

To further investigate the stability of bcc Cu, we performed two series of short (50 ps) simulations for a bcc system with the size of $25 \times 25 \times 25$ unit cells (31,250 atoms) and periodic or free boundary conditions applied in all directions. The simulations are performed for different values of temperature. In the case of the periodic boundary conditions, constant zero pressure is maintained during the simulations. We find that, when the periodic boundary conditions are applied, the bcc structure spontaneously transforms into a mixture of fcc and hcp close-packed structural regions at temperatures below 480 K. Above 480 K, the bcc structure remains stable for the duration of the simulations, 50 ps. With free boundary conditions, the bcc structure collapses into a mixture of fcc and hcp regions below 1,000 K and remains stable above 1,000 K. Thus, the bcc structure exhibits an increased stability with increasing temperature. The melting temperature of bcc Cu, determined using the same liquid-crystal coexistence method discussed in Sect. 2 for fcc Cu, yields the melting temperature of $1{,}262 \pm 3$ K, more than 20 K below that of the fcc Cu structure. The lower value of the melting temperature indicates that, despite the increase in the stability of the bcc Cu structure with increasing temperature, it remains a metastable non-equilibrium structure up to the melting temperature of the FBD EAM Cu material.

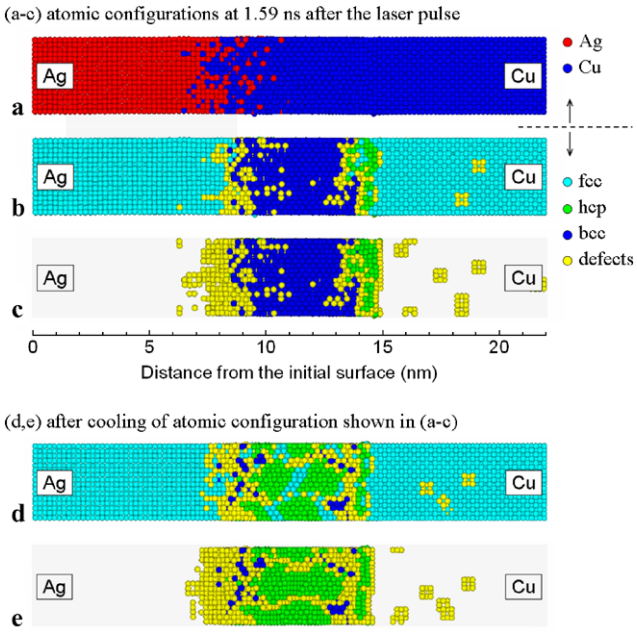

Fig. 6 Snapshots of the atomic configurations in a region adjacent to the Ag–Cu interface. The atomic configuration shown in (**a**)–(**c**) is obtained by the end of the simulation (1.59 ns after the laser pulse) and quenched by applying the velocity dampening technique for 0.2 ps. The atomic configuration shown in (**d**) and (**e**) is obtained by a gradual cooling (5 K/ps) of the system shown in (**a**)–(**c**). In (**a**), atoms are colored by their type: *red* for Ag and *blue* for Cu. In (**b**)–(**e**), atoms are colored according to the output of the structural analysis of [39] (see footnote 1): *light blue*, *green*, and *blue* atoms belong to local atomic configurations with fcc, hcp, and bcc/bct structures, respectively; the structure around the *yellow* atoms cannot be assigned to any crystal structure and is characteristic of point defects and dislocation cores. The fcc atoms are *blanked* in (**c**) and (**e**) to expose the defect structure. The region shown in (**a**)–(**c**) corresponds to the region for which the distributions of structural and physical characteristics are shown in Fig. 5. The snapshots shown in (**d**) and (**e**) are aligned with the ones in (**a**)–(**c**) to match the location of the lattice-mismatched interface

In the Cu–Ag target irradiated by the laser pulse, the epitaxial bcc Cu layer is stabilized by the presence of the underlying Ag (001) structure and remains stable during the cooling of the interfacial region down to 800 K (Fig. 3). The cooling rate in the combined TTM-MD simulation slows down with time and, to test the stability of the bcc structure upon further cooling more quickly, we performed a simulation of a faster cooling (with a rate of 5 K/ps) of the final atomic configuration obtained by the time of 1.59 ns in the TTM-MD simulation. In the simulation of the fast cooling, the bcc structure of the epitaxial layer remains stable down to the temperature of 300 K but transforms to a close-packed structure characterized by a mixture of hcp and fcc structural regions upon further cooling, Fig. 6d and e.

3.4 Structure of the runaway lattice-mismatched interface

Detailed analysis of the interface separating the pseudomorphic epitaxial layer of bcc Cu from the rest of the Cu sub-

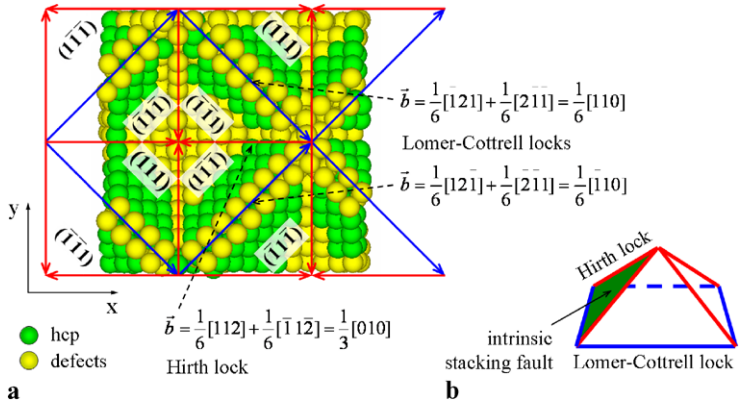

Fig. 7 Structure of the 'runaway' lattice-mismatched interface generated in the Ag–Cu system irradiated by a 200-fs laser pulse. The interface is located in the Cu substrate, below the Cu–Ag mixing region and the view from the side of the Cu substrate is shown in (**a**). Similarly to Fig. 6c, atoms are colored according to the local atomic structure, with *green* atoms located within the planes of intrinsic stacking faults in the fcc structure (local hcp configurations), *yellow* atoms cannot be assigned to any crystal structure and belong to the dislocation cores, and fcc atoms are blanked to expose the structure of the interface. The structure of the interface is represented by an array of stacking fault pyramids outlined by stair-rod partial dislocations. The lines of stair-rod partial dislocations in the base and at the edges of the pyramids (Lomer–Cottrell and Hirth locks, respectively) are shown by *blue* and *red arrows*. Examples of the dislocation reactions responsible for the formation of the locks are shown in the figure. A schematic representation of a structural element of the interfacial structure is shown in (**b**)

strate reveals a corrugated structure that has a thickness of ∼1.6 nm and is more complex compared to the plane array of $\frac{1}{2}\langle 110\rangle$ misfit dislocations shown in Fig. 1b for the original sharp semicoherent Cu–Ag interface. The atomic structure of the interface is shown in Fig. 7, where atoms are colored according to the local atomic structure and fcc atoms are blanked to expose the structure of the interface. The interface consists of a periodic array of stacking fault pyramids outlined by stair-rod partial dislocations [53], with the lateral periodicity of the array matching that of the original semicoherent interface, Fig. 1b. A schematic representation of a pyramid is shown in Fig. 7b. The partial dislocations in the base of each pyramid are identified as Lomer–Cottrell locks with $\vec{b} = \frac{1}{6}\langle 110\rangle$ and the partial dislocations forming the edges of the pyramids are Hirth locks with $\vec{b} = \frac{1}{3}\langle 010\rangle$. The faces of the pyramids are intrinsic stacking faults that show up as the layers of hcp atoms in Fig. 7a.

The interfacial structure consisting of the stacking fault pyramids can be considered as a product of dissociation of the original grid of perfect $\vec{b} = \frac{1}{2}\langle 110\rangle$ dislocations shown in Fig. 1b. The corresponding dislocation reactions can be illustrated by considering a perfect dislocation with $\vec{b} = \frac{1}{2}[110]$ and dislocation line oriented along the $[1\bar{1}0]$ direction (intersection of (111) and $(\bar{1}\bar{1}1)$ crystallographic planes). This dislocation can split into two perfect dislocations, $\frac{1}{2}[110] = \frac{1}{2}[011] + \frac{1}{2}[10\bar{1}]$, with the corresponding slip planes of $(\bar{1}\bar{1}1)$ and $(11\bar{1})$. These two dislocations can dissociate into two partial dislocations by the following reactions: $\frac{1}{2}[011] = \frac{1}{6}[112] + \frac{1}{6}[\bar{1}21]$ in the $(\bar{1}\bar{1}1)$ plane and $\frac{1}{2}[10\bar{1}] = \frac{1}{6}[2\bar{1}\bar{1}] + \frac{1}{6}[11\bar{2}]$ in the (111) plane. Then $\frac{1}{6}[\bar{1}21]$ can react with $\frac{1}{6}[2\bar{1}\bar{1}]$ to generate a Lomer–Cottrell lock at the intersection $[1\bar{1}0]$ of planes (111) and $(\bar{1}\bar{1}1)$ through the reaction $\frac{1}{6}[\bar{1}21] + \frac{1}{6}[2\bar{1}\bar{1}] = \frac{1}{6}[110]$ shown in Fig. 7a. Similarly, a Lomer–Cottrell lock at the intersection [110] of planes $(1\bar{1}\bar{1})$ and $(\bar{1}1\bar{1})$ can be generated through the reaction $\frac{1}{6}[12\bar{1}] + \frac{1}{6}[\bar{2}\bar{1}1] = \frac{1}{6}[\bar{1}10]$, etc. As an example of the generation of Hirth locks along the edges of the pyramids, a reaction $\frac{1}{6}[112] + \frac{1}{6}[\bar{1}\bar{1}2] = \frac{1}{3}[010]$ producing a stair-rod partial dislocation at the intersection $[\bar{1}0\bar{1}]$ of planes $(1\bar{1}\bar{1})$ and $(\bar{1}\bar{1}1)$ is also shown in Fig. 7a.

The formation of continuous stacking fault interfacial structures similar to the ones described above has been suggested in [54] for Cu–Ni interfaces subjected to tensile stresses in the plane of the interface. The results of Monte Carlo simulations performed for Ag–Cu interfaces [55, 56] also suggest that the (001) Cu–Ag interface is unstable against decomposition into {111} facets, which leads to the formation of Ag-rich pyramidal protrusions into the Cu-rich phase. The dissociation of the interface into the stacking fault pyramids creates a strong barrier to slip [54] and results in the effective hardening of the interfacial region.

4 Summary

The atomic mixing and structural transformations in a Ag film–Cu substrate system irradiated by a femtosecond laser pulse were investigated with a computational model that combines the classical MD method with a continuum description of laser excitation, electron–phonon equilibration, and electron heat conduction. The initial energy redistribution and the location/depth of the region undergoing melt-

ing and resolidification are strongly affected by the difference in the strength of electron–phonon coupling of the film and substrate materials and by the transient variations of the electron–phonon coupling related to the thermal excitation of lower band electrons. The higher strength of the electron–phonon coupling in Cu compared to Ag results in a *preferential sub-surface heating and melting of the Cu substrate*.

The steep temperature gradient and fast electronic heat conduction in Cu result in a very high cooling rate, up to $\sim 3 \times 10^{11}$ K/s, and create the conditions of strong undercooling in the melted region. Although the velocity of epitaxial regrowth of the Cu substrate reaches its maximum value of $\sim$100 m/s, the complete resolidification of the melted part of the target takes almost a nanosecond and the temperature of the interfacial region drops to values that are close to the eutectic temperature of the Cu–Ag system. At these temperatures, the second resolidification front starts to propagate from the side of the Ag film, crosses the mixing region, and meets the first resolidification front moving from the Cu side. As a result of this resolidification process, the new *lattice-mismatched interface is separated from the Ag–Cu mixing region and shifted into the Cu substrate*.

Detailed analysis of the structure of the resolidified part of the layered target indicates that the Cu–Ag mixing region is separated from the new lattice-mismatched interface by an *intermediate 2-nm-wide pseudomorphic bcc Cu layer* that grows epitaxially from the (001) face of the fcc Ag film during the final stage of the resolidification process. The lattice-mismatched interface that separates the pseudomorphic epitaxial bcc Cu from the rest of the Cu substrate is found to have a complex *three-dimensional corrugated structure consisting of a periodic array of stacking fault pyramids* outlined by stair-rod partial dislocations (Lomer–Cottrell locks in the base of the pyramids and Hirth locks at the edges of the pyramids). The intermediate bcc layer and the stacking fault pyramid structure of the 'runaway' mismatched interface are likely to present a strong barrier for dislocation propagation, resulting in the *effective hardening of the layered structure treated by the laser irradiation*.

The concentration profiles in the atomic mixing region generated as a result of laser-induced melting and resolidification are more than five times wider compared to the width of the equilibrium interface in this immiscible system. Moreover, the preferential melting of the Cu substrate creates the conditions for the *formation of asymmetric concentration profiles*, with a more extensive diffusion of Ag atoms into the Cu substrate compared to the diffusion of Cu atoms into the Ag film.

Acknowledgements The work is supported by the National Science Foundation through Grant No. DMR-0907247 and the Air Force Office of Scientific Research through Grant No. FA9550-09-1-0245. The authors would like to thank Dr. Roland Hergenröder and Dr. Evgeny L. Gurevich of the Institute for Analytical Sciences in Dortmund, Germany for insightful and stimulating discussions.

References

1. Q. Feng, Y.N. Picard, H. Liu, S.M. Yalisove, G. Mourou, T.M. Pollock, Scr. Mater. **53**, 511 (2005)
2. T. Höche, D. Ruthe, T. Petsch, Appl. Phys. A **79**, 961 (2004)
3. J. Jia, M. Li, C.V. Thompson, Appl. Phys. Lett. **84**, 3205 (2004)
4. V. Margetic, K. Niemax, R. Hergenröder, Anal. Chem. **75**, 3435 (2003)
5. R.L. Harzic, N. Huot, E. Audouard, C. Jonin, P. Laporte, Appl. Phys. Lett. **80**, 3886 (2002)
6. C. Xie, Surf. Coat. Technol. **113**, 1 (1999)
7. T. Sameshima, S. Usui, Jpn. J. Appl. Phys. **26**, L1208 (1987)
8. E. Ohmura, I. Fukumoto, I. Miyamoto, Int. J. Jpn. Soc. Precis. Eng. **32**, 248 (1998)
9. D.S. Ivanov, L.V. Zhigilei, Phys. Rev. B **68**, 064114 (2003)
10. X.W. Wang, J. Phys. D: Appl. Phys. **38**, 1805 (2005)
11. A.K. Upadhyay, H.M. Urbassek, J. Phys. D: Appl. Phys. **38**, 2933 (2005)
12. C. Cheng, X. Xu, Phys. Rev. B **72**, 165415 (2005)
13. S.I. Anisimov, V.V. Zhakhovskii, N.A. Inogamov, K. Nishihara, Yu.V. Petrov, Appl. Surf. Sci. **253**, 6390 (2007)
14. B.J. Demaske, V.V. Zhakhovsky, N.A. Inogamov, I.I. Oleynik, Phys. Rev. B **82**, 064113 (2010)
15. Z. Lin, R.A. Johnson, L.V. Zhigilei, Phys. Rev. B **77**, 214108 (2008)
16. D.S. Ivanov, Z. Lin, B. Rethfeld, G.M. O'Connor, Th.J. Glynn, L.V. Zhigilei, J. Appl. Phys. **107**, 013519 (2010)
17. Z. Lin, E.M. Bringa, E. Leveugle, L.V. Zhigilei, J. Phys. Chem. C **114**, 5686 (2010)
18. L.V. Zhigilei, Z. Lin, D.S. Ivanov, J. Phys. Chem. C **113**, 11892 (2009)
19. D.A. Thomas, Z. Lin, L.V. Zhigilei, E.L. Gurevich, S. Kittel, R. Hergenröder, Appl. Surf. Sci. **255**, 9605 (2009)
20. Z. Lin, L.V. Zhigilei, V. Celli, Phys. Rev. B **77**, 075133 (2008)
21. P. Duwez, R.H. Willens, W. Klement, J. Appl. Phys. **31**, 1136 (1960)
22. R.K. Linde, J. Appl. Phys. **37**, 934 (1966)
23. S. Mader, A.S. Nowick, H. Widmer, Acta Metall. **15**, 203 (1967)
24. B. Cantor, R.W. Cahn, Scr. Metall. **10**, 318 (1976)
25. H.W. Sheng, G. Wilde, E. Ma, Acta Mater. **50**, 475 (2002)
26. M. von Allmen, E. Huber, A. Blatter, K. Affolter, Int. J. Rapid Solidif. **1**, 15 (1984/85)
27. S.I. Anisimov, B.L. Kapeliovich, T.L. Perel'man, Sov. Phys. JETP **39**, 375 (1974)
28. S.M. Foiles, M.I. Baskes, M.S. Daw, Phys. Rev. B **33**, 7983 (1986)
29. A.F. Voter, S.P. Chen, Mater. Res. Soc. Symp. Proc. **82**, 175 (1999)
30. E.B. Webb III, G.S. Grest, D.R. Heine, J.J. Hoyt, Acta Mater. **53**, 3163 (2005)
31. J.J. Hoyt, J.W. Garvin, E.B. Webb III, M. Asta, Model. Simul. Mater. Sci. Eng. **11**, 287 (2003)
32. R.C. Weast (ed.), *Handbook of Chemistry and Physics*, 64th edn. (CRC Press, Boca Raton, 1983)
33. R. Najafabadi, D.J. Srolovitz, E. Ma, M. Atzmon, J. Appl. Phys. **74**, 3144 (1993)
34. M. Asta, S.M. Foiles, Phys. Rev. B **53**, 2389 (1996)
35. J.P. Rogers III, P. Wynblatt, S.M. Foiles, M.I. Baskes, Acta Metall. Mater. **38**, 177 (1990)
36. L.V. Zhigilei, B.J. Garrison, Mater. Res. Soc. Symp. Proc. **538**, 491 (1999)
37. C. Schafer, H.M. Urbassek, L.V. Zhigilei, B.J. Garrison, Comput. Mater. Sci. **24**, 421 (2002)
38. N.W. Ashcroft, N.D. Mermin, *Solid State Physics* (Holt, Rinehart and Winston, New York, 1976)
39. G.J. Ackland, A.P. Jones, Phys. Rev. B **73**, 054104 (2006)

40. http://www.faculty.virginia.edu/CompMat/electron-phonon-coupling/
41. R.H.M. Groeneveld, R. Sprik, A. Lagendijk, Phys. Rev. B **51**, 11433 (1995)
42. K.C. Mills, B.J. Monaghan, B.J. Keene, Int. Mater. Rev. **41**, 209 (1996)
43. J. Hohlfeld, S.-S. Wellershoff, J. Güdde, U. Conrad, V. Jähnke, E. Matthias, Chem. Phys. **251**, 237 (2000)
44. C. Suárez, W.E. Bron, T. Juhasz, Phys. Rev. Lett. **75**, 4536 (1995)
45. E. Leveugle, D.S. Ivanov, L.V. Zhigilei, Appl. Phys. A **79**, 1643 (2004)
46. T.Q. Qiu, C.L. Tien, Int. J. Heat Mass Transf. **37**, 2789 (1994)
47. E.C. Bain, Trans. Am. Inst. Min. Metall. Eng. **70**, 25 (1924)
48. H. Li, D. Tian, J. Quinn, Y.S. Li, F. Jona, P.M. Marcus, Phys. Rev. B **43**, 6342 (1991)
49. M. Dietterle, T. Will, D.M. Kolb, Surf. Sci. **396**, 189 (1998)
50. Z.S. Pereira, E.Z. da Silva, Phys. Rev. B **79**, 115404 (2009)
51. J.R. Chelikowsky, M.Y. Chou, Phys. Rev. B **38**, 7966 (1988)
52. Z. Tang, M. Hasegawa, Y. Nagai, M. Saito, Phys. Rev. B **65**, 195108 (2002)
53. A. Kelly, G.W. Groves, P. Kidd, *Crystallography and Crystal Defects*, revised edn. (Wiley, Chichester, 2000)
54. R.G. Hoagland, T.E. Mitchell, J.P. Hirth, H. Kung, Philos. Mag. A **82**, 643 (2001)
55. P. Bacher, P. Wynblatt, S.M. Foiles, Acta Metall. Mater. **39**, 2681 (1991)
56. P. Bacher, G. Rao, P. Wynblatt, Comput. Mater. Sci. **1**, 42 (1992)